

Article

Sustainable Synthesis of N/S-Doped Porous Carbon from Waste-Biomass as Electroactive Material for Energy Harvesting

Suguna Perumal ^{1,†}, Somasundaram Chandra Kishore ^{2,†}, Raji Atchudan ^{3,*,†}, Ashok K. Sundramoorthy ^{4,†}, Muthulakshmi Alagan ⁵ and Yong Rok Lee ^{3,*}

¹ Department of Chemistry, Sejong University, Seoul 143747, Korea; suguna.perumal@gmail.com

² Department of Biomedical Engineering, Saveetha School of Engineering, Saveetha Institute of Medical and Technical Sciences (SIMATS), Saveetha Nagar, Chennai 602105, Tamil Nadu, India; schandrakishore30@gmail.com

³ School of Chemical Engineering, Yeungnam University, Gyeongsan 38541, Korea

⁴ Department of Prosthodontics, Saveetha Dental College and Hospitals, Saveetha Institute of Medical and Technical Sciences, Poonamallee High Road, Velappanchavadi, Chennai 600077, Tamil Nadu, India; ashokkumars.sdc@saveetha.com

⁵ Center for Environmental Management Laboratory, National Institute of Technical Teachers Training and Research, Chennai 600113, Tamil Nadu, India; almuthulakshmi@gmail.com

* Correspondence: atchudanr@yu.ac.kr (R.A.); yrlee@yu.ac.kr (Y.R.L.)

† These authors contributed equally to this work.

Abstract: It is absolutely essential to convert biomass waste into usable energy in a rational manner. This investigation proposes the economical synthesis of heteroatom (N and S)-doped carbon (ATC) from *Aesculus turbinata* seed as a natural precursor by carbonization at 800 °C. The final product obtained was characterized using field emission scanning electron microscopy with energy-dispersive X-ray spectroscopy, high-resolution transmittance electron microscopy, X-ray diffraction, Raman spectroscopy, nitrogen adsorption-desorption isotherms, attenuated total reflectance Fourier transform infrared spectroscopy, and X-ray photoelectron spectroscopy in order to investigate its structural property and chemical composition. The porous carbon achieved by this method contained oxygen, nitrogen, and sulfur from *Aesculus turbinata* seed and had pores rich in micropores and mesopores. Crystalline ATC obtained with a high surface area (560 m² g⁻¹) and pore size (3.8 nm) were exploited as electrode material for the supercapacitor. The electrochemical studies revealed a specific capacitance of 142 F g⁻¹ at a current density of 0.5 A g⁻¹ using 1 M H₂SO₄ as an electrolyte. ATC had exceptional cycling stability, and the capacitance retention was 95% even after 10,000 charge-discharge cycles. The findings show that ATC derived from biomass proved to be a potential energy storage material by converting waste biomass into a high-value-added item, a supercapacitor.

Keywords: *Aesculus turbinata*; waste-biomass; porous carbon; supercapacitor; energy harvesting



Citation: Perumal, S.; Chandra Kishore, S.; Atchudan, R.; Sundramoorthy, A.K.; Alagan, M.; Lee, Y.R. Sustainable Synthesis of N/S-Doped Porous Carbon from Waste-Biomass as Electroactive Material for Energy Harvesting. *Catalysts* **2022**, *12*, 436. <https://doi.org/10.3390/catal12040436>

Academic Editor: Vincenzo Baglio

Received: 18 March 2022

Accepted: 11 April 2022

Published: 13 April 2022

Publisher's Note: MDPI stays neutral with regard to jurisdictional claims in published maps and institutional affiliations.



Copyright: © 2022 by the authors. Licensee MDPI, Basel, Switzerland. This article is an open access article distributed under the terms and conditions of the Creative Commons Attribution (CC BY) license (<https://creativecommons.org/licenses/by/4.0/>).

1. Introduction

Environmental sustainability requires two key components: clean energy and environmental preservation [1,2]. However, natural resource depletion and declining fuel availability have become primary reasons for the energy shortage, which has developed into a severe challenge that requires immediate attention [3]. Furthermore, the massive progress of portable electronic gadgets and electric vehicles has created a crucial need for high-energy-density storage solutions [4]. This change demands a constant supply of clean energy sources right away. There is a compelling need to shift focus away from fossil fuels and turn toward biomass-derived materials for energy storage and conversion in the current context. Designing sustainable, efficient energy storage and conversion materials using biomass and biowaste as carbon precursors to reduce environmental problems has received a lot of attention in recent years [5]. Following that, significant efforts have been undertaken to develop novel eco-friendly, renewable energy, and conversion devices.

Supercapacitors (SCs) [6–9], lithium-ion batteries [10,11], and fuel cells [12,13] are examples of electrochemical energy storage devices that are viable choices for next-generation energy systems. Supercapacitors, which have a better power density, a faster charge-discharge rate, a long cycling life, an easy configuration, and a higher Coulombic efficiency, are among these devices that make a connection between capacitors and batteries. Supercapacitors are used in a variety of applications, including electric cars [14], portable electric devices [15], and smart electrical grids [16]. SCs or electrochemical capacitors (ECCs) are electrochemical energy storage technologies that are capable of providing or absorbing enormous power. The mechanism of charge getting stored in SCs happens mainly on the periphery of active electrode materials. Supercapacitors make use of two types of active electrode materials based on the phenomenon by which charge is stored. The electrode material in the large majority of SCs is carbon with a large specific surface area and porous nature. These SCs are known as electrochemical double-layer capacitors (EDLCs) [17]. Here, the charge is stored by collecting ions from the electrolyte on the surface of carbon electrodes during the electrochemical reaction. Therefore, no redox processes are required. The second type of material used in SCs is pseudocapacitive materials [18]. The electrochemical studies of these materials appear to deliver capacitance value analogous to a carbonaceous material. Nevertheless, the storage mechanism is different, as the energy storage is quick and undergoes reversible redox processes, which typically occur near the (sub)surface of the material.

SCs have power densities that are suitable for the majority of applications. The most challenging task concerned with these devices is to boost their energy density, which is usually found to be low in most devices. It can be enhanced by raising either the capacitance or the voltage. There are several methods for increasing capacitance. The carbon/electrolyte contact determines the capacitance of EDLCs. Thus, adjusting the pore size in carbon to match the size of the ions present in the electrolyte for better diffusion or functionalizing the carbon with electrochemically active surface groups can lead to maximum capacitance. In the case of pseudocapacitive materials, charges are stored at the surface or sub-surface of the electrode-active material by undergoing redox reactions that are very quick and reversible. It is intriguing to use surface redox reactions to improve material capacitance since the Faradaic capacitance resulting from the reduction and oxidation reactions is mostly higher than the EDLC, originating from the adsorption of ions on the carbon electrode surface. As a result, using nanostructured pseudocapacitive materials is one method for improving the capacitance of materials.

Porous carbon compounds made from waste biomass are gaining popularity due to their long-term viability and environmental benefits. Carbon materials with porous behavior are ubiquitous and used in several contemporary devices because of their enormous surface area and exceptional physical, chemical, thermal, mechanical, and electrical capabilities [19–21]. Due to the rising need for highly efficient energy storage devices, carbon materials are widely employed as potential electrode materials in many areas of the energy sector, such as for supercapacitors, lithium-ion batteries, fuel cells, solar cells, and hydrogen storage [22]. The carbon matrix has an exceptional conductivity, allowing for high power density and cycle stability.

Natural materials are frequently abundant, renewable, inexpensive, and environmentally beneficial when compared to produced templates and precursors. Currently, the use of natural biological components to produce carbon composites has risen in popularity. Cotton, sugarcane bagasse, corn straw, rice straw, garlic skin, sunflower seed shell, sugar, rice husks, shrimp shells, wheat straw, and other carbon-derived biomass wastes have all been employed as the precursor for carbon electrodes in supercapacitor devices [2,21,23–28]. Suppose the carbon in these biomass materials can be turned into as many carbon-based useable products as feasible. In that case, it will provide a novel approach to converting waste biomass into high-value-added items and an essential option for lowering NO_x and CO₂ emissions. Different heteroatoms, such as nitrogen (N), boron (B), phosphorus (P), oxygen (O), and sulfur (S), are used as carbon-doping elements in SCs applications. Among

them, N/S-doped carbon has gained considerable attention [29,30]. In N-doped carbon materials, there are four primary types of structural nitrogen configurations: pyrrolic nitrogen, pyridinic nitrogen, quaternary or graphitic nitrogen, and oxidized pyridinic nitrogen atoms. Among these, many types of nitrogen components are considered that they have electrochemically active locations. Apart from N, S is known as one of the highest reactive elements among heteroatom doping because of its unpaired electrons, wider bandgap due to its electron-withdrawing character, a slight difference in electronegativity with carbon, and easily polarizable nature. A series of Faradaic redox reactions occur on S-doped carbonaceous electrodes, leading to increased pseudocapacitance. Moreover, the use of N/S for energy storage applications such as SCs will reduce N/S waste and offer more economical solutions in the long run [31].

The main aim of this work is focused on the possible reuse of biowaste with cost-effectiveness. *Aesculus turbinata*, often known as Horse Chestnut, is a deciduous tree that grows up to 20 m tall, has large leaves, and is native to Europe. Aescin, a mixture of triterpenoid saponin, coumarin derivatives, flavonoids, and tannin, is among the active compounds found in the seed [32]. In this study, we investigate *Aesculus turbinata* seed as a base material for the synthesis of porous carbon and its implementation as active electrode material for SCs.

2. Results and Discussion

Figure 1 depicts the FESEM images of prepared ATC at various magnifications and their elemental compositions imaging. From the images shown in Figure 1a–d, it is clear that the structure of carbon has a granular shape with pillar-like morphology and a spongy appearance. Presumably, this physical shape of the ATC can bestow a porous structure, thus providing an opportunity to enhance the surface area of the material, making it suitable as an active material for electrode applications in SCs. While investigating the elemental mapping over the surface of ATC for the image shown in Figure 1e–h, it was found that heteroatoms, such as N, O, S, were present in addition to C and uniformly dispersed over the surface. In the images, the elements C, O, N, and S are represented by the colors green, red, yellow, and cyan blue, respectively. Furthermore, while overlapping the individual maps, Figure 1i depicts the occurrence of all the mentioned heteroatoms in one image. The presence of these heteroatoms can play a key role in enhancing the capacitance of the material by providing the pseudocapacitive behavior to the material. For acquiring a deep insight into the nanostructure of the obtained ATC, the TEM and HRTEM images were analyzed, as shown in Figure 2. The TEM images displayed the spongy, porous structure of ATC. Moreover, these micro images encompass areas of light and dark grey regions. The light grey regions in the carbon material could be attributed to the porous region where there is less interaction of the electron beam during the analysis due to the limpidness. The dense areas over the carbon layer could be due to the incorporation of porous carbon structure with heteroatoms into the framework of ATC. Examination of the high-resolution TEM micrograph depicted in Figure 2d clearly showcases the lattice plane of ATC with the presence of regular lattice spacing of 0.37 nm, authenticating that carbon is acceptably graphitic in nature [33]. These observations assume that the ATC possesses a crystalline carbon plane with a spongy appearance. This further gives strong evidence for ATC meeting the selection criterion for an electrode material in SCs because crystalline carbon present along with heteroatom can enhance the conductivity of the electrode for better capacitance.

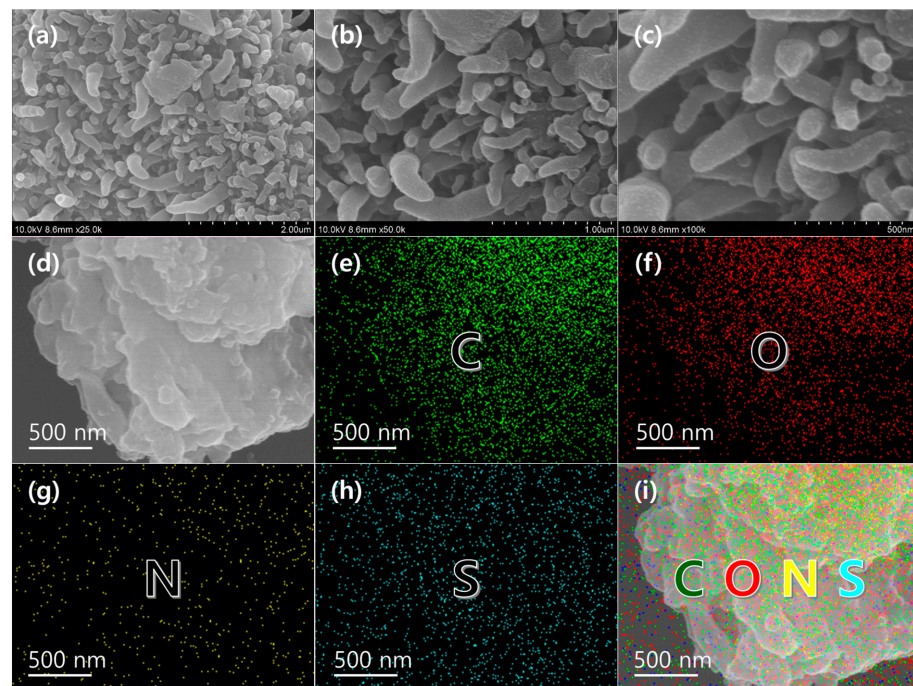


Figure 1. (a–d) FESEM images taken at various magnifications of the prepared ATC and the corresponding (e) carbon, (f) oxygen, (g) nitrogen, (h) sulfur, and (i) overlapping elemental maps of the presented elementals.

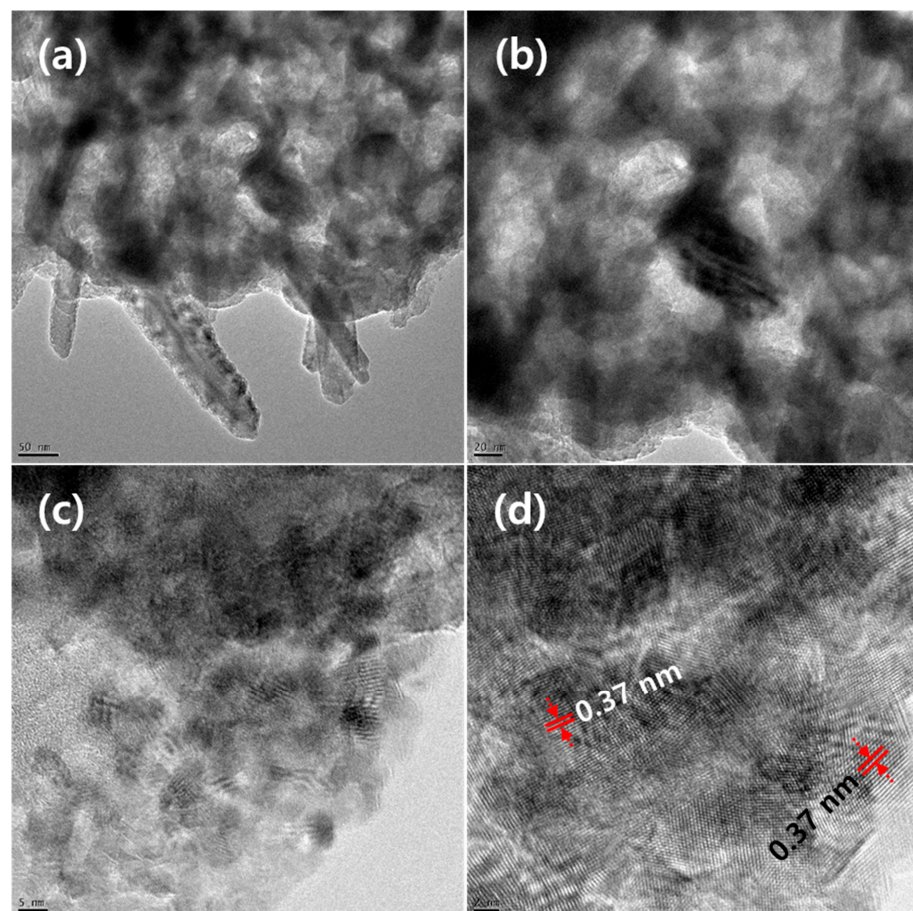


Figure 2. (a,b) TEM and (c,d) HRTEM images with different magnifications of the prepared ATC.

The X-ray diffraction (XRD) and Raman spectroscopy analyses were performed to study the crystallinity/graphitization of the obtained ATC. In Figure 3a, the XRD spectrum reveals two distinct, intense peaks centered at the incidence angle (2θ) 24° and 43° , indicating the formation of (002) and (100) crystal planes, respectively, corresponding to the characteristic peaks of graphitic carbon [34]. Moreover, the evaluation of the (002) peaks for determining the interplanar distance between the carbon lattice plane was performed using the Debye–Scherrer equation; and the value was calculated to be 0.37 nm. It was interesting to note that this theoretical value well coincides with the value (0.37 nm) obtained from HRTEM. Notably, this value seems to be higher when compared to the conventional graphene interplanar value of 0.34 nm. This variation in this value could be attributable to the fact that the doping of various heteroatom in the framework of carbon and the existence of functional groups on the surface can alter the interplanar spacing in the form of defects and deformations in carbon lattice planes. This assumption could be justified by the observations obtained from FESEM elemental mapping. Moreover, there are more chances for the occurrence of carbon surface oxidation that can eventually lead to the formation of partial amorphous coatings over ATC, which could also be a possible reason for the alteration in the interplanar spacing value. The formation of broad peaks at (002) can be considered as an authenticated proof for the formation of the amorphous nature or graphitic carbon sheets interconnected with edges/surface defects present in ATC. Further, the Raman spectrum obtained for ATC shown in Figure 3b was subjected to analysis. Two peaks in the spectrum formed at 1345 and 1590 cm^{-1} correspond to the existence of D-band (disorder) and G-band (graphitic carbon), respectively, present in ATC [35]. The intensity ratio of both bands (I_D/I_G) was determined to be 1, signifying the acceptable amount of graphitization present with the ATC structure. The disorder in the lattice plane could be attributed to the presence of various heteroatoms, such as N, S, and O functional groups, whereas the graphitic carbon framework with in-plane stretching vibrational mode related to sp^2 hybridized carbon is responsible for the G-band [35]. The spectrum also observed that both D and G bands had merged together with inadequate separation. Therefore, the predictions based on their intensities can provide only a rough value about the degree of graphitization. For a concrete result, the peak area was calculated for the degree of graphitization. Figure 3c shows the deconvoluted Raman spectrum of ATC, where the ratio of the area of D-band (A_D) and G-band (A_G) was calculated ($A_D/A_G = 1.3$). This value indicates moderate graphitization in ATC due to the presence of functional groups that leads to surface defects. However, this value shares a fair agreement with I_D/I_G obtained. The finding from these analyses thus well agrees with the TEM, HRTEM, and XRD results.

The surface area and porous nature of ATC were evaluated with Brunauer–Emmett–Teller (BET) surface area techniques. Figure 4a illustrates nitrogen adsorption-desorption isotherms of ATC. With reference to the IUPAC classification, the plot signifies a Brunauer–Deming–Deming–Teller (BDDT) type IV shape of the isotherms with an H3-type hysteresis loop, exhibiting the realization of micropores and mesopores. The assimilation of the hybrid mesoporous/microporous character of materials is indicated by the hysteresis loop generated by the significant adsorption of N_2 molecules in ATC, generated at low and high relative pressure (P/P_0) levels spanning the range 0.1–0.9. The BET-specific surface area for the sample was computed using nitrogen adsorption data and was found to be $560\text{ m}^2\text{ g}^{-1}$. The distribution of pore size in ATC was retrieved using the Barrett–Joyner–Halenda (BJH) approach. The existence of various porous structures, i.e., mesopores and micropores, is indicated by the pore size distribution curves of ATC illustrated in Figure 4b. The average size of the micropores and mesopores was estimated to be 1.8 nm and 3.8–40 nm, respectively. Furthermore, the ATC was observed to be inhabited by the majority of mesopores. The presence of this porosity in the ATC with moderate surface area is considered an essential feature for enhancing electrochemical reactions. This is possible by the rapid diffusion of electrolytes with less resistance and the presence of numerous active sites participating in the electrochemical reaction due to the high surface area. Having a moderate porous nature and surface area, ATC can thus be recommended

to be utilized as electrode material for EDLC. Eventually, ATC can store a massive amount of charge following the accumulation of numerous ionic species on the surface of the active material during the electrochemical reaction.

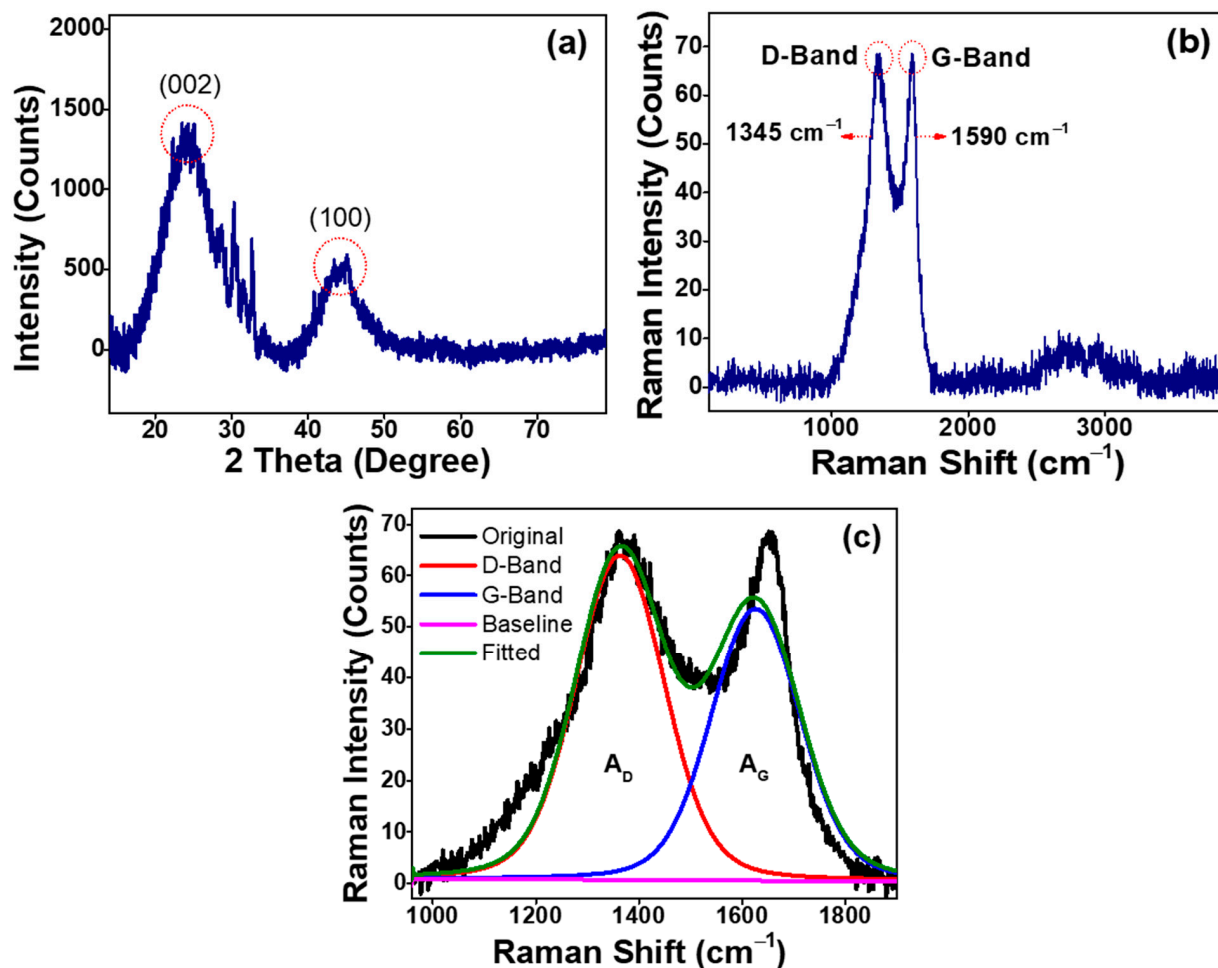


Figure 3. (a) XRD pattern, (b) Raman spectrum, and (c) Raman spectrum with area deconvolution of the prepared ATC.

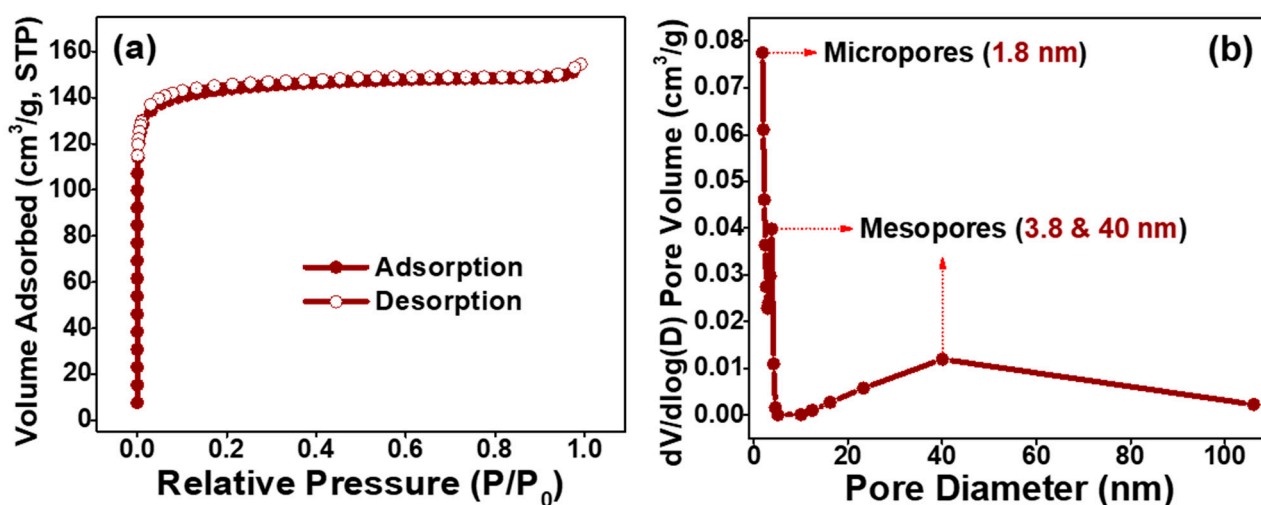


Figure 4. (a) Nitrogen adsorption-desorption isotherms of the prepared ATC and the corresponding (b) pore size distribution graph.

The functional groups attached over the surface of ATC were determined with the help of the attenuated total reflectance-Fourier transform infrared (ATR-FTIR) spectrum, as illustrated in Figure 5a. The spectrum reveals prominent peaks indicating the presence of vibration bands related to CH_2 , C-C-C/C-O-H , C-H/C-N , C=O/C=C , C-H , and -OH/NH moieties attached to the surface of ATC from the corresponding peaks formed around at 870, 1218, 1375, 1737, 2933, and 3300 cm^{-1} respectively [35–37]. The absorption peaks related to C-H bonds were found in the range of $2926\text{--}2935\text{ cm}^{-1}$. The absorption peak indicates the presence of C=O bonds at 1737 cm^{-1} . Notably, the presence of the C-N functional group accounts for the nitrogen species attached to ATC. Subsequently, these surface functional groups thus confirmed over ATC are considered very beneficial by promoting better dispersion and chemical stability for electrochemical reactions to enhance the capacitance of the supercapacitor. In addition, the X-ray photoelectron spectroscopy (XPS) spectrum shown in Figure 5b,c was employed to investigate the chemical composition and binding energy (BE) of ATC. In order to have better clarity of the overall elemental constituents present in ATC, the XPS survey spectrum was evaluated. Figure 5b clearly displays the survey spectrum evident for the presence of C 1s , N 1s , S 2p , and O 1s with the atomic percentage of 86, 2, 1, and 11, respectively. The high-resolution of the C 1s spectrum shown in Figure 5c is deconvoluted into three peaks with BE values 284.8, 285.9, and 287.1 eV denoting the carbon bonds C=C/C-C , C-OH/C-N , and O=C-OH , respectively [38,39]. Moreover, the spectrum in Figure 5d describes the deconvoluted spectrum of O 1s present in ATC, which is separated into three major peaks. The 531.2, 532.8, and 534 eV peaks signify the typical C=O , C-O , and O=C=O bonds, respectively [38,40]. The presence of these peaks could be attributed to the atmospheric water content absorbed on the surfaces of ATC. The magnified spectrum shown in Figure 5e represents the N 1s level fitted into three different peaks with BE values of 398.5, 400.9, and 403.5 eV signifying pyridinic-N (C-N-C), pyrrolic-N (C-N-H), and graphitic-N ($(\text{C})_3\text{-N}$), respectively, as various nitrogen bonding states with carbon in ATC [41]. The C-N configurations (pyridinic-N and pyrrolic-N) contribute one or two electrons, respectively, to π at carbon sp^2 as delocalized electrons. The delocalized electron is excited to π^* bonds at sp^2 C with the π electron of the sp^2 C. Therefore, the excited electrons recombine with holes in the π bonds at sp^2 C. Furthermore, the high-resolution XPS deconvoluted spectra of S 2p are shown in Figure 5f and are split into three peaks. The oxidized sulfur, $\text{S 2p}_{3/2}$, and $\text{S 2p}_{1/2}$ states are represented by three sub-peaks produced at the BE of 164.3, 167.8, and 169.6 eV, respectively [42]. This finding supports the heteroatom doping of S and N atoms into the carbon framework to improve the carbon composite electrode's wettability and electrical conductivity [43].

The cyclic voltammetry (CV) curves at different scan rates ($5\text{--}100\text{ mV s}^{-1}$) and galvanostatic charge-discharge (GCD) curves at different current densities ($0.5\text{--}3.0\text{ A g}^{-1}$) of ATC in a three-electrode system are shown in Figure 6a,b, respectively. The CV curves exhibit stable quasi-rectangular shapes at lower scan rates, representing the ideal EDLC capacitive behavior and good reversibility for the electrolyte ions diffusing rapidly to the electrode interface [44,45]. Besides, the morphology of the CV curve departs to some extent from its quasi-rectangular shapes with increasing scan rates, and the area of the cyclic voltammogram increased with increasing the scan rates, demonstrating the existence of partial diffusion resistance and ideal capacitive behavior. At the low scan rate, ions in the electrolyte might diffuse microporous and mesoporous structures of ATC, besides increasing the scan rate, providing insufficient time for the accessibility of ions towards ATC microstructure. The GCD curves exhibit nearly triangular shapes and are reasonably symmetrical even as the current density is elevated to 3 A g^{-1} , indicating the good Coulombic efficiency with superior electrochemical double-layer capacitor (EDLC) performance of ATC [46]. Moreover, the GCD exhibits a larger potential window, and the larger area under the GCD curve was noticed, authenticating its higher energy storage ability. The specific capacitance (C_s) is measured to be 142, 107, 87, 70, 57, and 49 F g^{-1} at the current densities of 0.5, 1.0, 1.5, 2.0, 2.5, and 3.0 A g^{-1} , respectively, using equation (1) as shown in Figure 6c. Figure 6c reveals that the ATC can retain 35% of its specific capacitance as the current

density was raised from 0.5 to 3 A g⁻¹, demonstrating the outstanding rate capability of the active electrode materials. The electrochemical behavior of the ATC active electrode material was studied based on the electrochemical impedance spectroscopy (EIS) performance and the Nyquist plot of EIS of ATC shown in Figure 6d. The equivalent circuit diagram employed for the fitting of the EIS data is represented in the inset of Figure 6d, which comprises the equivalent series resistance, the charge transfer resistance, and the double-layer capacitance. The EIS is fitted using an equivalent circuit of $R_1 + Q_2/R_2 + Q_3/R_3$ by Z-View software. The solution resistance (R_1 , 2.6 Ω cm⁻²), charge-transfer resistance (R_2 , 28.4 Ω cm⁻²), and the coating resistance (R_3 , 2811 Ω cm⁻²) were calculated from the Nyquist plots fit. The capacitances, including Q_2 and Q_3 of ATC, are calculated as 0.31 and 0.44 F cm⁻², respectively. The obtained Nyquist plot displays a distorted semicircle at high-frequency besides a nearly vertical line where charge saturation dominates. It was observed from the Nyquist plot in the high-frequency region that the Z'-intercept on the x-axis signifies a value of 2.6 Ω cm⁻² for the series resistance, demonstrating a good power density for the device [47]. Besides, the smaller distorted semicircle of ATC suggests a lower charge-transfer resistance and a more efficient ion diffusion process between the interface of the electrode and the electrolyte solution. This efficient charge transfer process between the electrolyte and electrode interface confirms a large capacitance and good rate capability. The nearly vertical line of the Nyquist plot in the low-frequency region suggests better capacitive behavior due to the non-faradaic charge storage mechanism of ATC [48]. Moreover, the synthesized ATC reveals an acceptable specific capacitance value that can be attributed to the higher specific surface area and the functionalized surface of the ATC, which is the fascinating portion of the charge-discharge process [49].

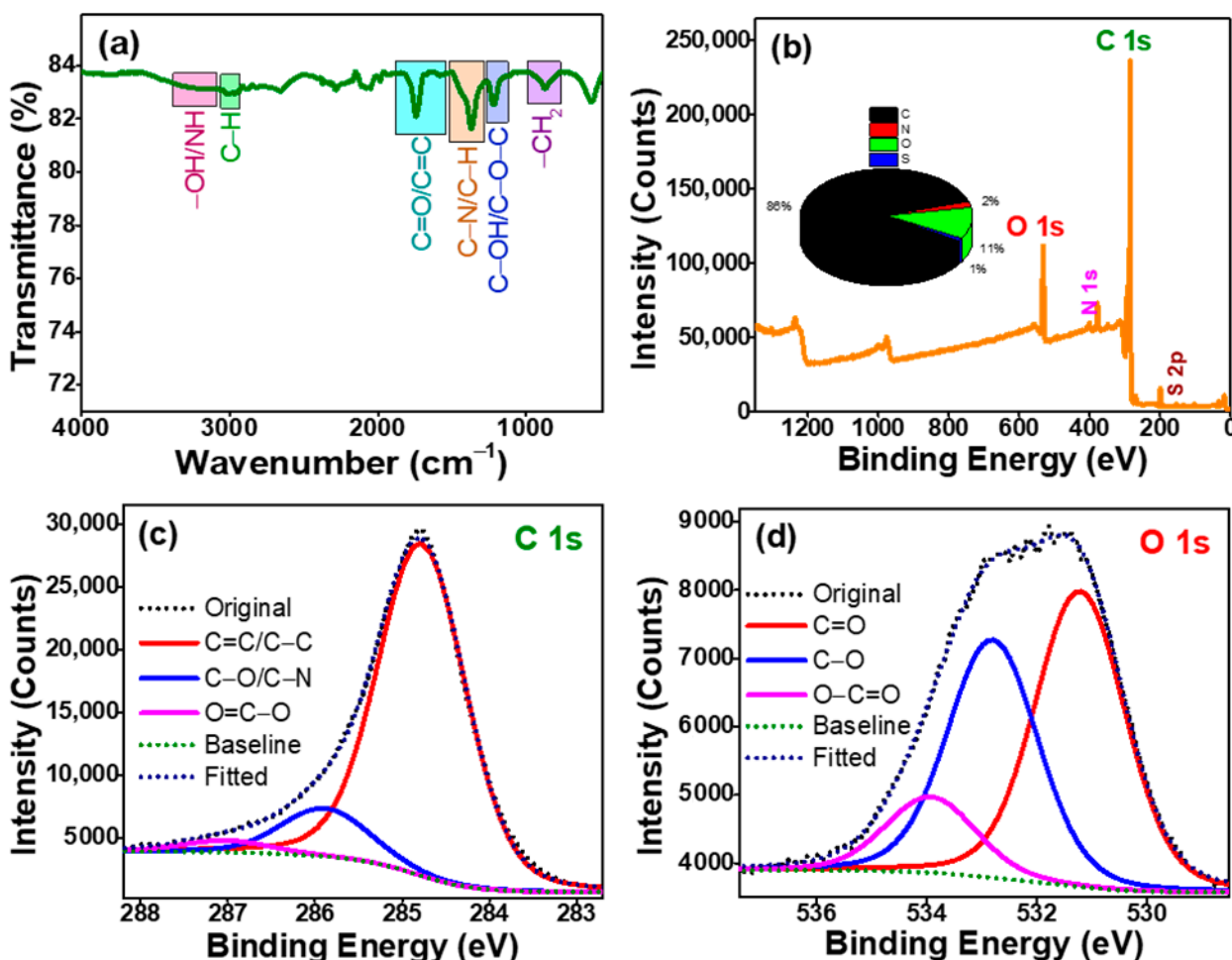


Figure 5. Cont.

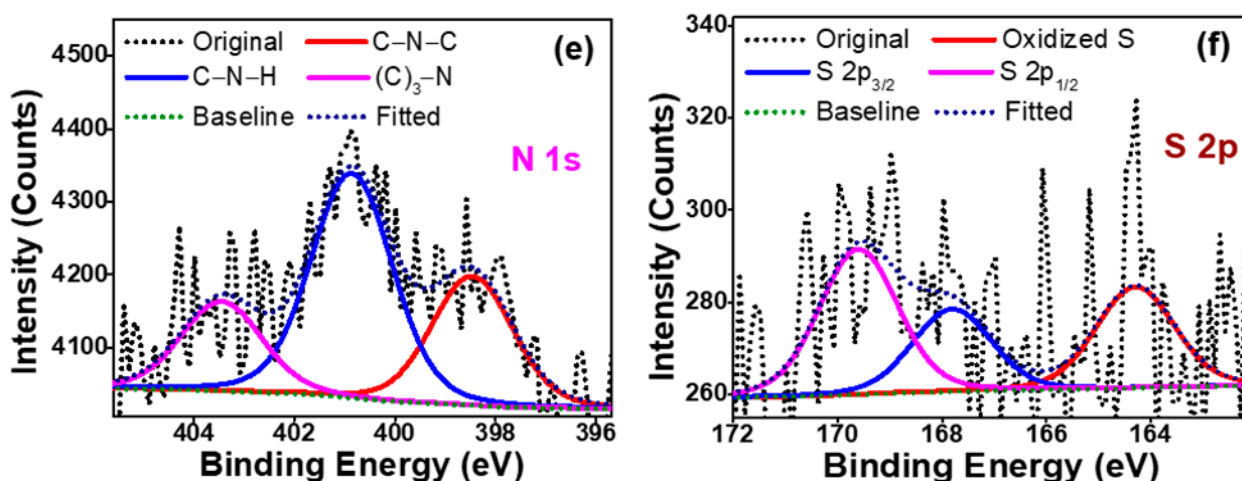


Figure 5. (a) ATR-FTIR and (b) XPS spectrum of the prepared ATC (inset: elemental composition chart of ATC). High-resolution XPS spectra (c) C 1 s, (d) O 1 s, (e) N 1 s, and (f) S 2p of ATC.

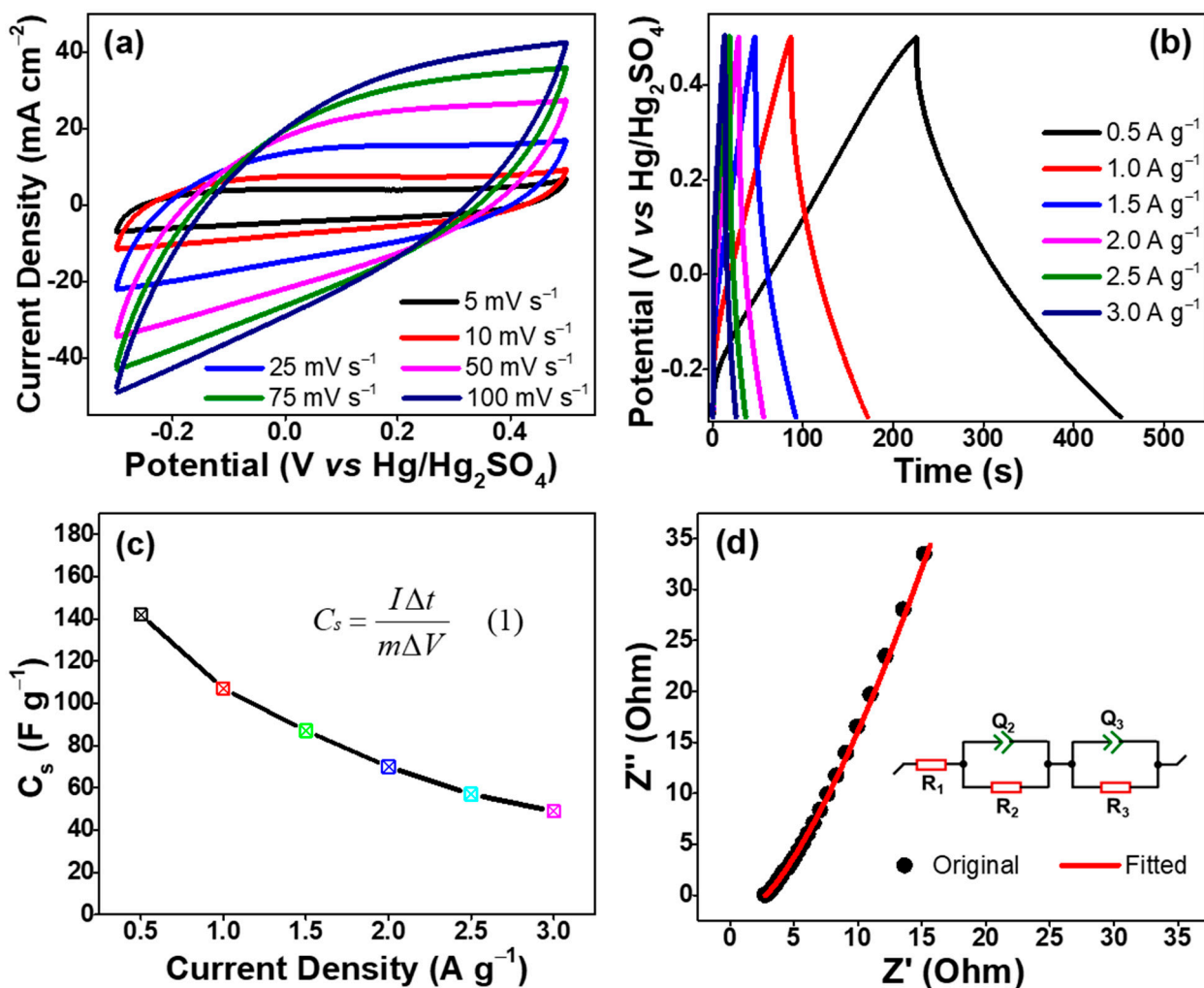


Figure 6. Electrochemical performance of ATC: (a) CV curves, (b) GCD curves, (c) C_s at various current densities (inset: equation for the calculation of specific capacitances (C_s)), and (d) Nyquist plot with suitable circuit diagram.

Moreover, long-term cycling stability is one of the crucial parameters for assessing the practical application of active electrode materials (symmetric energy storage devices). Figure 7a presents a cycling stability plot of the ATC where GCD cycling measurement was performed at a current density of 2 A g^{-1} in a three-electrode system. The figure revealed that ATC had excellent cycling stability, and the capacitance retention was 95% even after 10,000 charge-discharge cycles. The excellent cycling stability can be credited to the high stability of the ATC and the interface between the electrode and the electrolyte and was suitable for use in supercapacitors [44]. After cycle stability, the electrochemical measurements, including CV and GCD, were performed in the three-electrode system. They were compared with the initial CV and GCD curves at a scan rate of 25 mV s^{-1} and a current density of 0.5 A g^{-1} , which are presented in Figure 7b,c, respectively. Surprisingly, the ATC shows an unchangeable CV and GCD curves even after 10,000 charge-discharge cycles. These results suggest that the ATC material is very stable under the acidic condition and becomes more capacitive due to the osmosis of electrolytes through the pores in the ATC electrode [45]. Such excellent stabilities, such as cycling and chemical stability, can be attributed to the spongy-like porous architecture and carbon framework. The pores were exposed to the electrolyte, offering sufficient diffusion channels. Table 1 shows the comparison of the present work with the previously reported literature on carbon-based materials from various natural resources. It was observed that the present work delivered a moderate result with respect to other biowaste precursors.

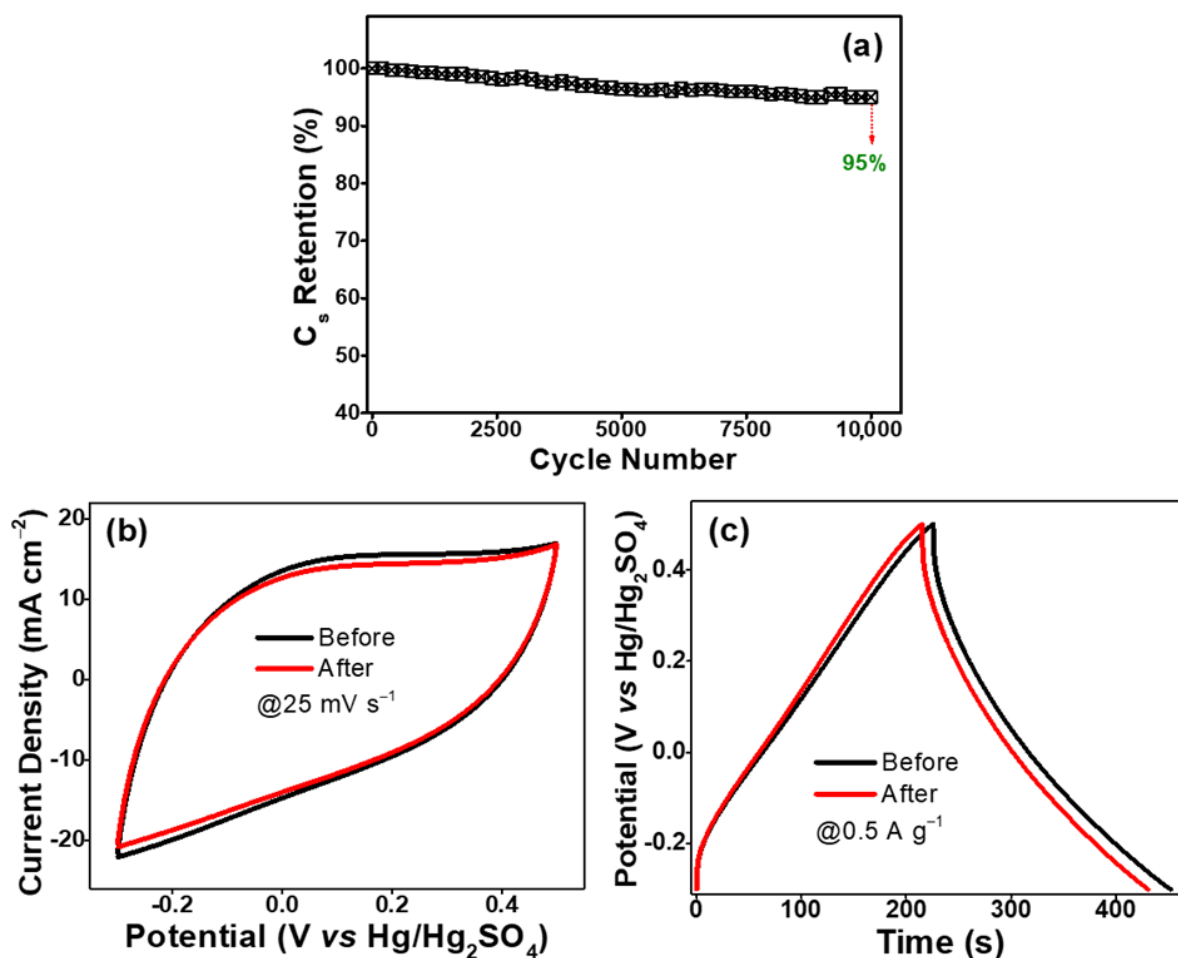


Figure 7. Electrochemical performance of ATC: (a) cycle performance, (b) CV curves comparison, and (c) GCD curves comparison.

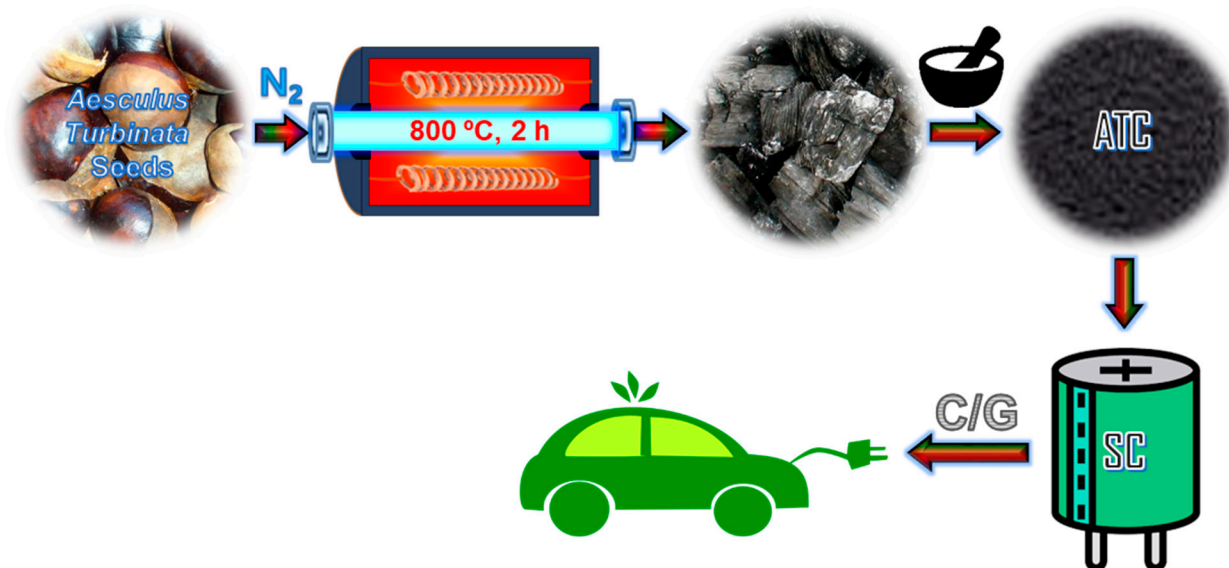
Table 1. Comparison of present work with the previously reported literature on carbon-based materials from various natural resources.

Precursor	Synthesis Method	Electrolyte Solution	C _s (F g ⁻¹)/CD (A g ⁻¹)	Cycle/Retention (%)	Reference
Banana peel	carbonization	1 M H ₂ SO ₄	137/0.5	10,000/94	[50]
Palm kernel shell	carbonization	1 M KOH	210/0.5	1000/97	[51]
Peanut shell	carbonization	1 M H ₂ SO ₄	340/1.0	10,000/95.3	[52]
Watermelon rind	carbonization	6 M KOH	333.4/1.0	10,000/96.8	[53]
Bamboo	carbonization	3 M KOH	293/0.5	10,000/91.8	[54]
Wheat straw	citric-acid-crosslinking	(PVA)/KOH	200/10	5000/97.6	[55]
Chestnut-pulp	carbonization	6 M KOH	373/0.5	10,000/99.7	[56]
Human hair	carbonization	1 M H ₂ SO ₄	274.5/1.0	10,000/87	[57]
Lotus stalk	carbonization	6 M KOH	248.5/1.0	5000/90.6	[58]
Lotus fruit	carbonization	1 M H ₂ SO ₄	160/0.5	10,000/95	[24]
Corn starch	carbonization	6 M KOH	144/0.6	3000/99	[59]
<i>A. turbinata</i> seed	carbonization	1 M H ₂ SO ₄	142/0.5	10,000/95	This work

3. Materials and Methods

Preparation of ATC Material

Aesculus turbinata seeds were collected, washed, and dried at 100 °C under atmospheric air conditions. The dried *Aesculus turbinata* seeds were carbonized by placing them in the middle of a tubular furnace, where the temperature was maintained at 800 °C for 2 h under the nitrogen ambiance. The resulting ATC is a black product grounded well with a motor and pestle. It was later subjected to various characterizations to study the physical and chemical properties and implications as an electrode in supercapacitors. The detailed synthesis and application of ATC materials are shown in Scheme 1. More descriptions about materials, instrumentation methods, fabrication of working electrode, and electrochemical measurements of the prepared ATC material are shown in Supplementary Materials.

**Scheme 1.** Schematic illustration for the formation of ATC from *Aesculus turbinata* seed via the one-step pyrolysis method and their energy storage applications.

4. Conclusions

In summary, the porous carbon ATC from *Aesculus turbinata* seeds can be successfully prepared by a simple one-step pyrolysis method. The studies based on structural characterization and chemical composition analysis show that the ATC has a hybrid micro/mesoporous structure with a sufficient BET surface area, appropriate heteroatom (S and N)-doping, and a reasonable degree of graphitization/crystallization. The presence

of various functional groups, such as CH₂, C–O–C/C–O–H, C–H/C–N, C=C, C–H, and –OH/NH, moieties can enhance the dispersion and chemical wettability/stability of ATC. The crystalline nature of ATC with high surface area and heteroatoms plays an integrated role in improving the capacitance of the active material. The as-prepared ATC has the specific capacitance of 142 F g^{−1} at the current density of 1.0 A g^{−1} in an aqueous solution of 1 M H₂SO₄. ATC had excellent cycling stability even after 10,000 charge-discharge cycles with robust capacitance retention of 95%. Altogether, the ATC generated from *Aesculus turbinata* seeds could be used as a renewable, cost-effective, and high-performance electroactive material for supercapacitors, as per the findings. Furthermore, this work offers a solid example of converting waste biomass into a valuable energy-storage material, providing helpful guidelines for managing biowaste/biomass towards improved environmental preservation.

Supplementary Materials: The following are available online at <https://www.mdpi.com/article/10.3390/catal12040436/s1>, materials, instrumentation methods, fabrication of working electrode, and electrochemical measurements of the prepared ATC material.

Author Contributions: Conceptualization, methodology, visualization, and writing—review & editing, S.P.; investigation and writing—original draft, S.C.K.; conceptualization, data curation, formal analysis, investigation, and writing—original draft, R.A.; visualization and investigation, A.K.S.; validation and visualization, M.A.; project administration and supervision, Y.R.L. All authors equally contributed to this work. All authors have read and agreed to the published version of the manuscript.

Funding: This work was supported by the National Research Foundation of Korea (NRF) grant funded by the Korean government MSIT (2021R1A2B5B02002436).

Data Availability Statement: Not applicable.

Acknowledgments: Authors thank the National Research Foundation of Korea (NRF) for providing financial support.

Conflicts of Interest: The authors declare no conflict of interest.

References

1. Yi, H. Clean energy policies and green jobs: An evaluation of green jobs in US metropolitan areas. *Energy Policy* **2013**, *56*, 644–652. [[CrossRef](#)]
2. Vinodh, R.; Sasikumar, Y.; Kim, H.-J.; Atchudan, R.; Yi, M. Chitin and chitosan based biopolymer derived electrode materials for supercapacitor applications: A critical review. *J. Ind. Eng. Chem.* **2021**, *104*, 155–171. [[CrossRef](#)]
3. Harris, J.M.; Roach, B. *Environmental and Natural Resource Economics: A Contemporary Approach*; Routledge: New York, NY, USA, 2017.
4. Ovshinsky, S.; Fetcenko, M.; Ross, J. A nickel metal hydride battery for electric vehicles. *Science* **1993**, *260*, 176–181. [[CrossRef](#)] [[PubMed](#)]
5. Njoku, C.E.; Ike, I.S.; Adediran, A.A.; Nwaeju, C.C. The Place of Biomass-Based Electrode Materials in Next-Generation Energy Conversion and Storage. In *Electrode Materials for Energy Storage and Conversion*; CRC Press: Boca Raton, FL, USA, 2021; pp. 229–261.
6. Shao, Y.; El-Kady, M.F.; Sun, J.; Li, Y.; Zhang, Q.; Zhu, M.; Wang, H.; Dunn, B.; Kaner, R.B. Design and mechanisms of asymmetric supercapacitors. *Chem. Rev.* **2018**, *118*, 9233–9280. [[CrossRef](#)]
7. González, A.; Goikolea, E.; Barrena, J.A.; Mysyk, R. Review on supercapacitors: Technologies and materials. *Renew. Sustain. Energy Rev.* **2016**, *58*, 1189–1206. [[CrossRef](#)]
8. Pandolfo, A.G.; Hollenkamp, A.F. Carbon properties and their role in supercapacitors. *J. Power Sources* **2006**, *157*, 11–27. [[CrossRef](#)]
9. Edison, T.N.J.I.; Atchudan, R.; Karthik, N.; Chandrasekaran, P.; Perumal, S.; Arunachalam, P.; Raja, P.B.; Sethuraman, M.G.; Lee, Y.R. Electrochemically exfoliated graphene sheets as electrode material for aqueous symmetric supercapacitors. *Surf. Coat. Technol.* **2021**, *416*, 127150. [[CrossRef](#)]
10. Kim, T.; Song, W.; Son, D.-Y.; Ono, L.K.; Qi, Y. Lithium-ion batteries: Outlook on present, future, and hybridized technologies. *J. Mater. Chem. A* **2019**, *7*, 2942–2964. [[CrossRef](#)]
11. Manthiram, A. Materials challenges and opportunities of lithium ion batteries. *J. Phys. Chem. Lett.* **2011**, *2*, 176–184. [[CrossRef](#)]
12. Carrette, L.; Friedrich, K.A.; Stimming, U. Fuel cells: Principles, types, fuels, and applications. *ChemPhysChem* **2000**, *1*, 162–193. [[CrossRef](#)]
13. Dyer, C.K. Fuel cells for portable applications. *J. Power Sources* **2002**, *106*, 31–34. [[CrossRef](#)]

14. Horn, M.; MacLeod, J.; Liu, M.; Webb, J.; Motta, N. Supercapacitors: A new source of power for electric cars? *Econ. Anal. Policy* **2019**, *61*, 93–103. [[CrossRef](#)]
15. Zhao, C.; Liu, Y.; Beirne, S.; Razal, J.; Chen, J. Recent development of fabricating flexible micro-supercapacitors for wearable devices. *Adv. Mater. Technol.* **2018**, *3*, 1800028. [[CrossRef](#)]
16. Cai, G.; Darmawan, P.; Cui, M.; Wang, J.; Chen, J.; Magdassi, S.; Lee, P.S. Highly stable transparent conductive silver grid/PEDOT:PSS electrodes for integrated bifunctional flexible electrochromic supercapacitors. *Adv. Energy Mater.* **2016**, *6*, 1501882. [[CrossRef](#)]
17. Sharma, P.; Bhatti, T. A review on electrochemical double-layer capacitors. *Energy Convers. Manag.* **2010**, *51*, 2901–2912. [[CrossRef](#)]
18. Jiang, Y.; Liu, J. Definitions of pseudocapacitive materials: A brief review. *Energy Environ. Mater.* **2019**, *2*, 30–37. [[CrossRef](#)]
19. Xie, L.; Su, F.; Xie, L.; Guo, X.; Wang, Z.; Kong, Q.; Sun, G.; Ahmad, A.; Li, X.; Yi, Z. Effect of pore structure and doping species on charge storage mechanisms in porous carbon-based supercapacitors. *Mater. Chem. Front.* **2020**, *4*, 2610–2634. [[CrossRef](#)]
20. Vijayan, B.L.; Mohd Zain, N.K.; Misnon, I.I.; Reddy, M.V.; Adams, S.; Yang, C.-C.; Anilkumar, G.M.; Jose, R. Void space control in porous carbon for high-density supercapacitive charge storage. *Energy Fuels* **2020**, *34*, 5072–5083. [[CrossRef](#)]
21. Bi, Z.; Kong, Q.; Cao, Y.; Sun, G.; Su, F.; Wei, X.; Li, X.; Ahmad, A.; Xie, L.; Chen, C.-M. Biomass-derived porous carbon materials with different dimensions for supercapacitor electrodes: A review. *J. Mater. Chem. A* **2019**, *7*, 16028–16045. [[CrossRef](#)]
22. Yuan, K.; Hu, T.; Xu, Y.; Graf, R.; Brunklaus, G.; Forster, M.; Chen, Y.; Scherf, U. Engineering the morphology of carbon materials: 2D porous carbon nanosheets for high-performance supercapacitors. *ChemElectroChem* **2016**, *3*, 822–828. [[CrossRef](#)]
23. Sudhan, N.; Subramani, K.; Karnan, M.; Ilayaraja, N.; Sathish, M. Biomass-derived activated porous carbon from rice straw for a high-energy symmetric supercapacitor in aqueous and non-aqueous electrolytes. *Energy Fuels* **2017**, *31*, 977–985. [[CrossRef](#)]
24. Atchudan, R.; Edison, T.N.J.I.; Perumal, S.; Vinodh, R.; Babu, R.S.; Sundramoorthy, A.K.; Renita, A.A.; Lee, Y.R. Facile synthesis of nitrogen-doped porous carbon materials using waste biomass for energy storage applications. *Chemosphere* **2022**, *289*, 133225. [[CrossRef](#)] [[PubMed](#)]
25. Edison, T.N.J.I.; Atchudan, R.; Sethuraman, M.G.; Lee, Y.R. Supercapacitor performance of carbon supported Co₃O₄ nanoparticles synthesized using Terminalia chebula fruit. *J. Taiwan Inst. Chem. Eng.* **2016**, *68*, 489–495. [[CrossRef](#)]
26. Xu, P.; Tong, J.; Zhang, L.; Yang, Y.; Chen, X.; Wang, J.; Zhang, S. Dung beetle forewing-derived nitrogen and oxygen self-doped porous carbon for high performance solid-state supercapacitors. *J. Alloy Compd.* **2022**, *892*, 162129. [[CrossRef](#)]
27. Atchudan, R.; Edison, T.N.J.I.; Perumal, S.; Thirukumaran, P.; Vinodh, R.; Lee, Y.R. Green synthesis of nitrogen-doped carbon nanograss for supercapacitors. *J. Taiwan Inst. Chem. Eng.* **2019**, *102*, 475–486. [[CrossRef](#)]
28. Atchudan, R.; Edison, T.N.J.I.; Perumal, S.; Lee, Y.R. Green synthesis of nitrogen-doped graphitic carbon sheets with use of Prunus persica for supercapacitor applications. *Appl. Surf. Sci.* **2017**, *393*, 276–286. [[CrossRef](#)]
29. Lu, H.; Liu, S.; Zhang, Y.; Huang, Y.; Zhang, C.; Liu, T. Nitrogen-Doped Carbon Polyhedra Nanopapers: An Advanced Binder-Free Electrode for High-Performance Supercapacitors. *ACS Sustain. Chem. Eng.* **2019**, *7*, 5240–5248. [[CrossRef](#)]
30. Liu, X.; Mi, R.; Yuan, L.; Yang, F.; Fu, Z.; Wang, C.; Tang, Y. Nitrogen-Doped Multi-Scale Porous Carbon for High Voltage Aqueous Supercapacitors. *Front. Chem.* **2018**, *6*, 475. [[CrossRef](#)]
31. Shaheen Shah, S.; Abu Nayem, S.M.; Sultana, N.; Saleh Ahammad, A.J.; Abdul Aziz, M. Preparation of Sulfur-doped Carbon for Supercapacitor Applications: A Review. *ChemSusChem* **2022**, *15*, e202101282. [[CrossRef](#)]
32. Sato, I.; Suzuki, T.; Kobayashi, H.; Tsuda, S. Antioxidative and antigenotoxic effects of Japanese horse chestnut (*Aesculus turbinata*) seeds. *J. Vet. Med. Sci.* **2005**, *67*, 731–734. [[CrossRef](#)]
33. Cao, Y.; Xiao, L.; Sushko, M.L.; Wang, W.; Schwenzler, B.; Xiao, J.; Nie, Z.; Saraf, L.V.; Yang, Z.; Liu, J. Sodium ion insertion in hollow carbon nanowires for battery applications. *Nano Lett.* **2012**, *12*, 3783–3787. [[CrossRef](#)] [[PubMed](#)]
34. Gizem Güneştekin, B.; Medetalibeyoglu, H.; Atar, N.; Lütfi Yola, M. Efficient Direct-Methanol Fuel Cell Based on Graphene Quantum Dots/Multi-walled Carbon Nanotubes Composite. *Electroanalysis* **2020**, *32*, 1977–1982. [[CrossRef](#)]
35. Titus, E.; Ali, N.; Cabral, G.; Gracio, J.; Babu, P.R.; Jackson, M. Chemically functionalized carbon nanotubes and their characterization using thermogravimetric analysis, fourier transform infrared, and raman spectroscopy. *J. Mater. Eng. Perform.* **2006**, *15*, 182–186. [[CrossRef](#)]
36. Tong, X.; Qin, Y.; Guo, X.; Moutanabbir, O.; Ao, X.; Pippel, E.; Zhang, L.; Knez, M. Enhanced catalytic activity for methanol electro-oxidation of uniformly dispersed nickel oxide nanoparticles—Carbon nanotube hybrid materials. *Small* **2012**, *8*, 3390–3395. [[CrossRef](#)] [[PubMed](#)]
37. Atchudan, R.; Jebakumar Immanuel Edison, T.N.; Perumal, S.; Lee, Y.R. Indian gooseberry-derived tunable fluorescent carbon dots as a promise for in vitro/in vivo multicolor bioimaging and fluorescent ink. *ACS Omega* **2018**, *3*, 17590–17601. [[CrossRef](#)]
38. Dam, D.T.; Wang, X.; Lee, J.-M. Graphene/NiO nanowires: Controllable one-pot synthesis and enhanced pseudocapacitive behavior. *ACS Appl. Mater. Interfaces* **2014**, *6*, 8246–8256. [[CrossRef](#)] [[PubMed](#)]
39. Atchudan, R.; Edison, T.N.J.I.; Aseer, K.R.; Perumal, S.; Karthik, N.; Lee, Y.R. Highly fluorescent nitrogen-doped carbon dots derived from Phyllanthus acidus utilized as a fluorescent probe for label-free selective detection of Fe³⁺ ions, live cell imaging and fluorescent ink. *Biosens. Bioelectron.* **2018**, *99*, 303–311. [[CrossRef](#)] [[PubMed](#)]
40. Krishnaiah, P.; Atchudan, R.; Perumal, S.; Salama, E.-S.; Lee, Y.R.; Jeon, B.-H. Utilization of waste biomass of Poa pratensis for green synthesis of n-doped carbon dots and its application in detection of Mn²⁺ and Fe³⁺. *Chemosphere* **2022**, *286*, 131764. [[CrossRef](#)]
41. Atchudan, R.; Edison, T.N.J.I.; Perumal, S.; Vinodh, R.; Lee, Y.R. Betel-derived nitrogen-doped multicolor carbon dots for environmental and biological applications. *J. Mol. Liq.* **2019**, *296*, 111817. [[CrossRef](#)]

42. Eda, G.; Yamaguchi, H.; Voiry, D.; Fujita, T.; Chen, M.; Chhowalla, M. Photoluminescence from chemically exfoliated MoS₂. *Nano Lett.* **2011**, *11*, 5111–5116. [[CrossRef](#)]
43. Cheng, Y.; Wu, L.; Fang, C.; Li, T.; Chen, J.; Yang, M.; Zhang, Q. Synthesis of porous carbon materials derived from laminaria japonica via simple carbonization and activation for supercapacitors. *J. Mater. Res. Technol.* **2020**, *9*, 3261–3271. [[CrossRef](#)]
44. Zhang, H.; Xu, L.; Liu, G. Synthesis of Benzoxazine-Based N-Doped Mesoporous Carbons as High-Performance Electrode Materials. *Appl. Sci.* **2020**, *10*, 422. [[CrossRef](#)]
45. Cai, J.; Lv, C.; Watanabe, A. High-performance all-solid-state flexible carbon/TiO₂ micro-supercapacitors with photo-rechargeable capability. *RSC Adv.* **2017**, *7*, 415–422. [[CrossRef](#)]
46. Jin, H.; Zhou, L.; Mak, C.L.; Huang, H.; Tang, W.M.; Chan, H.L.W. Improved performance of asymmetric fiber-based micro-supercapacitors using carbon nanoparticles for flexible energy storage. *J. Mater. Chem. A* **2015**, *3*, 15633–15641. [[CrossRef](#)]
47. Singh, S.; Sahoo, R.K.; Shinde, N.M.; Yun, J.M.; Mane, R.S.; Kim, K.H. Synthesis of Bi₂O₃-MnO₂ nanocomposite electrode for wide-potential window high performance supercapacitor. *Energies* **2019**, *12*, 3320. [[CrossRef](#)]
48. Sahu, V.; Shekhar, S.; Ahuja, P.; Gupta, G.; Singh, S.K.; Sharma, R.K.; Singh, G. Synthesis of hydrophilic carbon black; role of hydrophilicity in maintaining the hydration level and protonic conduction. *RSC Adv.* **2013**, *3*, 3917–3924. [[CrossRef](#)]
49. Bhardwaj, P.; Kaushik, S.; Gairola, P.; Gairola, S.P. Polyaniline enfolded hybrid carbon array substrate electrode for high performance supercapacitors. *J. Polym. Eng.* **2019**, *39*, 228–238. [[CrossRef](#)]
50. Raji, A.; Thomas Nesakumar, J.I.E.; Mani, S.; Perumal, S.; Rajangam, V.; Thirunavukkarasu, S.; Lee, Y.R. Biowaste-originated heteroatom-doped porous carbonaceous material for electrochemical energy storage application. *J. Ind. Eng. Chem.* **2021**, *98*, 308–317. [[CrossRef](#)]
51. Misnon, I.I.; Zain, N.K.M.; Abd Aziz, R.; Vidyadharan, B.; Jose, R. Electrochemical properties of carbon from oil palm kernel shell for high performance supercapacitors. *Electrochim. Acta* **2015**, *174*, 78–86. [[CrossRef](#)]
52. Wei, X.; Wan, S.; Jiang, X.; Wang, Z.; Gao, S. Peanut-shell-like porous carbon from nitrogen-containing poly-N-phenylethanolamine for high-performance supercapacitor. *ACS Appl. Mater. Interfaces* **2015**, *7*, 22238–22245. [[CrossRef](#)]
53. Mo, R.-J.; Zhao, Y.; Wu, M.; Xiao, H.-M.; Kuga, S.; Huang, Y.; Li, J.-P.; Fu, S.-Y. Activated carbon from nitrogen rich watermelon rind for high-performance supercapacitors. *RSC Adv.* **2016**, *6*, 59333–59342. [[CrossRef](#)]
54. Zhang, G.; Chen, Y.; Chen, Y.; Guo, H. Activated biomass carbon made from bamboo as electrode material for supercapacitors. *Mater. Res. Bull.* **2018**, *102*, 391–398. [[CrossRef](#)]
55. Du, W.; Zhang, Z.; Du, L.; Fan, X.; Shen, Z.; Ren, X.; Zhao, Y.; Wei, C.; Wei, S. Designing synthesis of porous biomass carbon from wheat straw and the functionalizing application in flexible, all-solid-state supercapacitors. *J. Alloy Compd.* **2019**, *797*, 1031–1040. [[CrossRef](#)]
56. Zhang, D.; Sun, L.; Liu, Q.; Sun, H.; Wang, Q.; Li, W.; Li, Z.; Wang, B. Ultra-high specific surface area porous carbon derived from chestnut for high-performance supercapacitor. *Biomass Bioenergy* **2021**, *153*, 106227. [[CrossRef](#)]
57. Dubey, P.; Shrivastav, V.; Kaur, A.; Maheshwari, P.H.; Sundriyal, S. Surface and Diffusion Charge Contribution Studies of Human Hair-Derived Heteroatom-Doped Porous Carbon Electrodes for Supercapacitors. *Energy Fuels* **2021**, *36*, 626–637. [[CrossRef](#)]
58. Zhang, L.; Yuan, J.; Su, S.; Cui, Y.; Shi, W.; Zhu, X. Porous active carbon derived from lotus stalk as electrode material for high-performance supercapacitors. *J. Wood Chem. Technol.* **2021**, *41*, 46–57. [[CrossRef](#)]
59. Pang, L.; Zou, B.; Zou, Y.; Han, X.; Cao, L.; Wang, W.; Guo, Y. A new route for the fabrication of corn starch-based porous carbon as electrochemical supercapacitor electrode material. *Colloids Surf. A Physicochem. Eng. Asp.* **2016**, *504*, 26–33. [[CrossRef](#)]